PCCP

ROYAL SOCIETY OF CHEMISTRY

PAPER

View Article Online
View Journal | View Issue

Cite this: *Phys. Chem. Chem. Phys.*, 2021, **23**, 17279

Gate-tunable superconductivity and charge-density wave in monolayer 1T′-$MoTe_2$ and 1T′-WTe_2†

Jun-Ho Lee ‡ and Young-Woo Son *

Received 19th May 2021,
Accepted 21st July 2021

DOI: 10.1039/d1cp02214h

rsc.li/pccp

Using first-principles calculation methods, we reveal a series of phase transitions as a function of gating or electron doping in monolayered quantum spin Hall (QSH) insulators, 1T′-$MoTe_2$ and 1T′-WTe_2. With increasing electron doping, we show that a phonon mediated superconducting phase is realized first and is followed by a charge density wave (CDW) phase with a nonsymmorphic lattice symmetry. The newly found CDW phase exhibits Weyl energy bands with spin–orbit coupling with fractional band filling, and reforms into a topological nontrivial phase with fully filled bands. The robust resurgence of the QSH state coexisting with the CDW phase is shown to originate from band inversions induced by the nonsymmorphic lattice distortion through the strong electron–phonon interaction, thus suggesting the realization of various interfacial states between superconducting states, and various CDW and topological states on a two-dimensional crystal by inhomogeneous gating or doping.

1 Introduction

Layered transition metal dichalcogenides (TMDs) have shown collective phenomena alongside topological electronic properties. Prominent examples are charge density wave (CDW),[1] superconducting (SC) phases,[2] the two-dimensional (2D) quantum spin Hall (QSH) state,[3] and three-dimensional (3D) Weyl semimetal (WSM) state,[4] to name a few. Among these, CDW and SC in bulk TMDs have been studied over several decades.[1,2] Recently, there have been intensive efforts to understand the new physical properties shown in a single-layer limit of TMDs that may differ from those in their bulk form.[5–12]

Maintaining their stoichiometry, TMDs have several polymorphic structures showing radically different electronic properties.[13] The most common atomic structures are the trigonal prismatic (2H) and octahedral (1T) form. For single-layer $MoTe_2$ and WTe_2, the 1T structure is unstable and turns into the distorted octahedral structure called the 1T′ form.[3,14] For many other TMDs, the 1T′ structure has not been observed as it is a metastable structure. Recently, novel synthetic approaches have been developed and 1T′ structures for other TMDs have also been realized.[12] One of the most fascinating phenomena shown in the 1T′ structure is the emergence of topologically nontrivial states. For example, the 2D QSH state in a single-layer 1T′ structure is theoretically predicted[3] and was experimentally confirmed recently.[15–19]

The aforementioned distinct states could be enhanced, intertwined, or made to coexist by external perturbations such as chemical or carrier doping.[20–25] Doping- or edge-induced phase transitions between different polymorphic structures for 2H and 1T forms have been studied theoretically[26–29] and experimentally,[30,31] while those for single-layer 1T′ structures have not been studied well. As the 1T′-TMDs have shown various topological states differing from 2H and 1T forms, there is interesting interplay between carrier doping, structural phase transition, collective phenomena and topological states. Recently, there have been theoretical studies on doping-induced superconductivity in monolayer 1T′-WTe_2 [32,33] assuming inversion symmetry. Although a pristine 1T′-WTe_2 preserves the inversion symmetry, experiments on superconductivity[9–11] were performed using the gating that breaks the inversion symmetry, lifting degeneracy in electronic structure and phonon dispersion. As the proposed mechanisms for the superconductivity assumed inversion symmetry, the lifting degeneracy may lead to a different mechanism for the superconductivity such as Ising pairing.[34] Thus, it should be revisited considering the effect of gating. Motivated by rapid developments in this field realizing extremely thin samples,[15–18,31] we have performed a comprehensive theoretical study on possible phase transitions as a function of external gating in single-layer 1T′-$MoTe_2$ and 1T′-WTe_2.

Korea Institute for Advanced Study, 85 Hoegiro, Seoul 02455, Korea.
E-mail: hand@kias.re.kr, junholee@berkeley.edu

† Electronic supplementary information (ESI) available: Acoustic phonon dispersion of MoTe along XM line. Comparison of energetics of 2 × 5 and 2 × 8 CDW phases. Projected band structures of 2 × 5 CDW. Effect of tensile strain to the band structure of the 2 × 5 CDW. See DOI: 10.1039/d1cp02214h

‡ Present address: Department of Physics, University of California, Berkeley, CA 94720, USA.

In this work, using various first-principles calculation methods, we explore a series of phase transitions in single-layer 1T′-$MoTe_2$ and 1T′-WTe_2 (henceforth $MoTe_2$ and WTe_2 for simplicity), with a field-effect transistor (FET) gating setup.[35] We find that the phase transitions in the 1T′-TMDs differ from those shown in other TMDs. Without doping, single-layer 1T′ TMDs are QSH insulators.[3] We show that with low doping, a phonon-mediated SC phase with a maximum transition temperature (T_c) of 9 K could be realized. With increasing doping, we find that the SC phase fades away and that a new CDW phase emerges. The crystal structures in the newly found CDW phase are distorted in such a way as to respect the nonsymmorphic lattice symmetry, which leads to 2D Weyl semimetallic energy bands with spin–orbit coupling.[36] We also find that a topological QSH state appears again when the energy bands of the new CDW phase are fully filled. So, the coexistence of the QSH state and CDW phase are predicted. As the doping concentrations considered in this study have already been achieved in recent experiments,[22,23,25] we believe that various interesting interfacial structures between the SC phase, CDW states and topological insulator properties,[37–40] can be manipulated on single-layer 1T′-TMDs by external doping or gating.

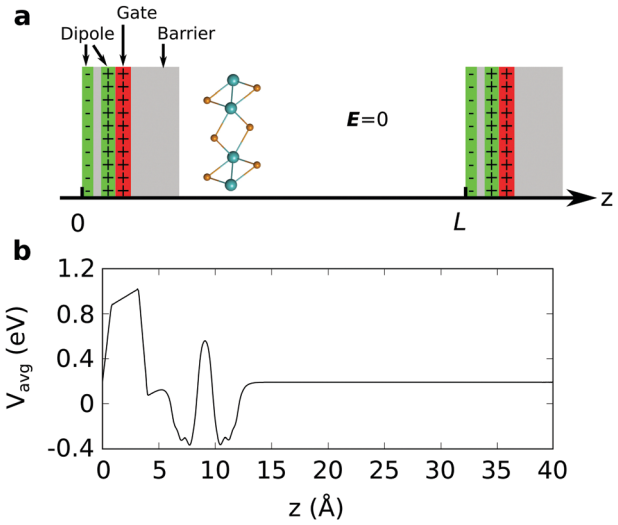

Fig. 1 (a) Schematic figure of the field effect transistor gating with the atomic structure of the 1T′-transition metal dichalcogenide (TMD). The atomic structure is viewed along the chalcogen chain direction. The length of the unit cell along z is given by L. (b) Plane-averaged potential profile where we used the vacuum region of ~27 Å. The sharp peak of V_{avg} around ~8 Å corresponds to the position of the transition metals of TMD. The barrier between the fictitious gate and TMD is in between the vacuum and TMD.

2 Computational methods

We performed density-functional theory calculations using a quantum espresso package.[41,42] We used the PBE generalized gradient approximation[43] for the exchange–correlation functional with scalar and fully relativistic optimized norm-conserving pseudopotentials from the PseudoDojo library.[44] We used 80 Ry planewave energy cutoff. We simulated the electron and hole doping by realistic modeling of the FET gating geometry as shown in Fig. 1a.[35] The dipole for the dipole correction is placed at $z_{dip} = d_{dip}/2$ with $d_{dip} = 0.02L$, with L being the unit-cell size in the direction perpendicular to the 2D plane. The charged plane modeling the gate electrode was placed close to the dipole at $z_{mono} = 0.021L$. A potential barrier with a height of $V_0 = 2.5$ Ry and a width of $d_b = 0.1L$ was used. We used the epw package to compute the Eliashberg equation and electron–phonon coupling (EPC) with fine grids.[45,46] The k-point integration was done with $10 \times 20 \times 1$ ($5 \times 4 \times 1$ and $5 \times 10 \times 1$) Monkhorst–Pack scheme for a 1×1 (2×5 and 2×2) cell of 1T′ phase. Structural relaxation was performed until the Hellmann–Feynman forces on all the atoms and total energy change became less than 10^{-4} a.u. and 10^{-6} a.u. simultaneously. The vacuum region between adjacent slabs is ~15 Å. The Methfessel–Paxton scheme for smearing is used with 0.02 Ry of Gaussian spreading. We used the density-functional perturbation theory (DFPT) to calculate the phonon-dispersion relation with $4 \times 8 \times 1$ q-point grids with a threshold for self-consistency of 10^{-18} Ryd. The electronic wave functions required for the Wannier interpolation within epw are calculated on uniform and Γ-centered $4 \times 8 \times 1$ k-point grids. For the initial guess of Wannierization, 22 Wannier functions, five d-orbitals for two Mo (W) atoms and three p-orbitals for four Te atoms, are used to describe the electronic structure. In order to solve the Eliashberg equations, we evaluated electron energies, phonon frequencies, and electron–phonon matrix elements on fine grids using the methods in ref. 47. The fine grids contain $20 \times 40 \times 1$ k and q-points. The frequency cutoff (ω_c) is set to 1 eV. The Eliashberg spectral function considered here reads

$$\alpha^2F(\omega) = \frac{1}{2}\int_{BZ}\frac{d\mathbf{q}}{\Omega_{BZ}}\omega_{\mathbf{q}\nu}\lambda_{\mathbf{q}\nu}\delta(\omega - \omega_{\mathbf{q}\nu}), \quad (1)$$

and the corresponding EPC strength is

$$\lambda = \int_0^\infty \frac{\alpha^2F(\omega)}{\omega}d\omega, \quad (2)$$

where $\lambda_{\mathbf{q}\nu}$ and $\omega_{\mathbf{q}\nu}$ are the EPC strength and frequency associated with a phonon mode ν and wavevector $\mathbf{q}$. From the calculated λ, we estimated the transition temperature (T_c) of the superconducting phase using the Allen–Dynes formula:

$$T_c = \frac{\omega_{log}}{1.2}\exp\left(-\frac{1.04(1+\lambda)}{\lambda - \mu_c^*(1+0.62\lambda)}\right), \quad (3)$$

where ω_{log} is a logarithmic average of the phonon frequency, μ_c^* is the Coulomb pseudopotential with 0.16. We neglect the effect of the spin–orbit coupling (SOC) in computing EPC.

3 Results

First, we computed the equilibrium lattice parameters of $MoTe_2$ (WTe_2) as $a = 6.380$ (6.331) Å and $b = 3.457$ (3.495) Å, which are consistent with previous theoretical studies.[3,32] Then, we calculated electronic band structures with and without SOC as

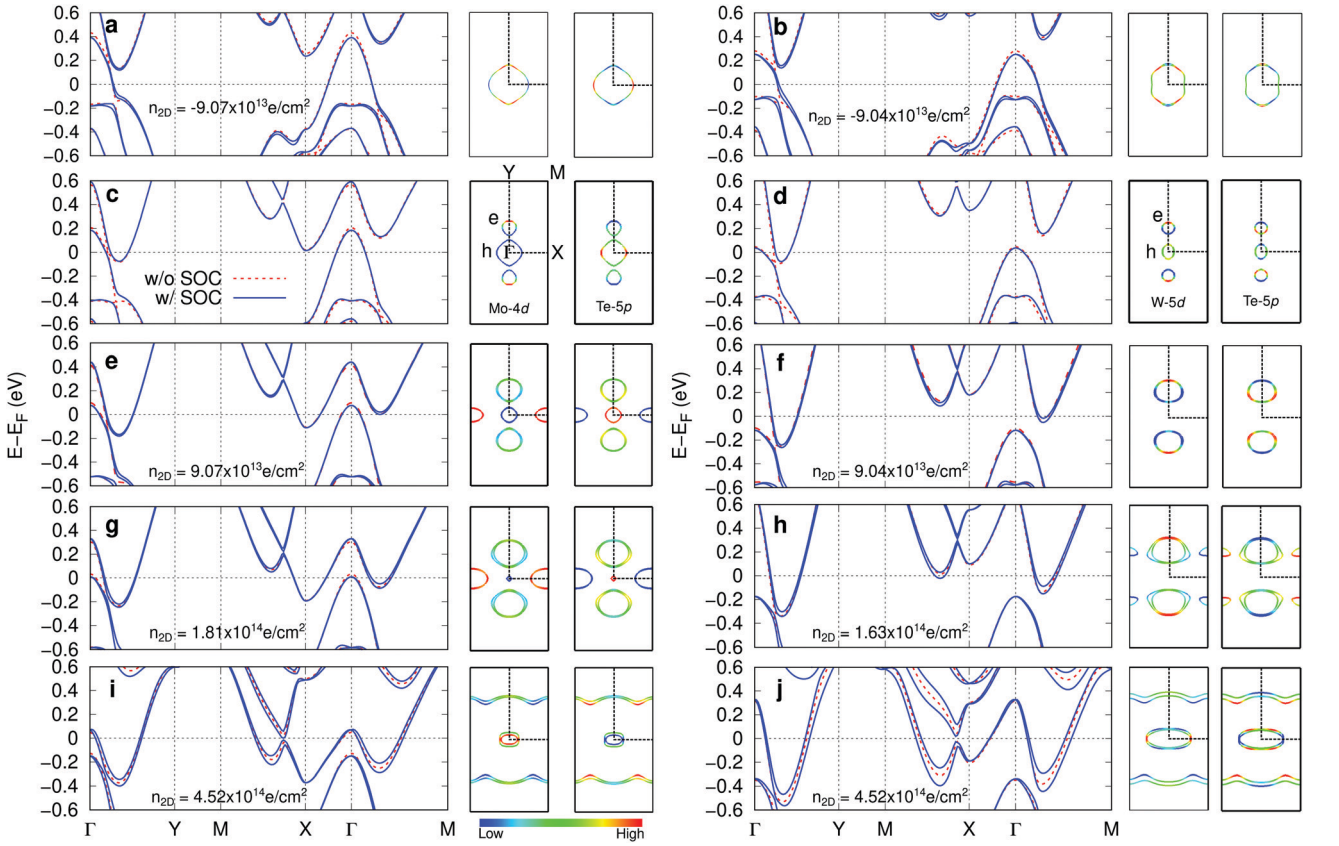

Fig. 2 Band structure and Fermi surface (FS) of monolayer (c) 1T′-$MoTe_2$ and (d) 1T′-WTe_2. The blue solid (red-dashed) line is calculated with (without) spin–orbit coupling. The middle and right panels are Mo(W) d and Te p orbitals projected Fermi surfaces, respectively. (e), (g), and (i) are band structures and FSs of $MoTe_2$ are calculated by several n_{2D}. (f), (h), and (i) are band structures and FSs of WTe_2 are calculated by several n_{2D}. (a) and (b) are electronic structures with the hole doping for $MoTe_2$ and WTe_2, respectively.

shown in Fig. 2(c) and (d), confirming that the inclusion of SOC suppresses a crossing point and provides the nontrivial topological Z_2 invariant, a hallmark of the QSH state. Fermi surfaces (FSs) are composed of a hole pocket centered at the Γ point and electron pockets located on the ΓY line. We projected the FSs onto Mo (W) 4d (5d) and Te 5p orbitals using FermiSurfer.[48] For $MoTe_2$, the electron (hole) pockets can be characterized by the Mo 4d (Te 5p), while for WTe_2 the W 5d and Te 5p are more hybridized in the electron and the hole pockets because of the different configuration of the valences of Mo and W in the vicinity of FS.[49] For both cases the orbital distributions are highly anisotropic.

On top of that, we applied the FET gating using the methods described in the previous section. The doping concentration (n_{2D}) can be defined as $n_{2D} = x/A$ in electrons per cm^2, where x is the amount of electrons added to the unit cell and A is the area of the unit cell. Fig. 2(a), (b) and (e)–(j) represent band structures and FSs for several n_{2D}. Fermi energy (E_F) shifts up (down) by electron (hole) doping and the bandwidth and the relative energies between bands slightly changes as well. For the bands with SOC the degeneracy of the energy bands is lifted due to inversion symmetry breaking in the FET gating. This can be seen in the 2D plane-averaged potential profile along the z-axis where the potential profile is asymmetric with respect to TMD as shown in Fig. 1(b). The spin splitting increases with increasing n_{2D} and is highly momentum dependent. For WTe_2 the splitting is more significant than that of $MoTe_2$ because of the more substantial SOC effect. The corresponding FS also changes a lot. For the case of hole doping, the electron pocket at Γ point disappears and the size of the hole pocket increases for both $MoTe_2$ and WTe_2. The size of the hole pocket at Γ point decreases with electron doping and eventually disappears. For $MoTe_2$, the area of electron pocket located on the ΓY line increases with doping and a new electron pocket featuring the strong d-character emerges at the X point. For WTe_2, similar behavior is shown while an electron pocket with p-character develops on the XM line earlier than the electron pocket with d-character at the X point. In higher n_{2D} ($\sim 4.52 \times 10^{14}$ e cm^{-2}), for both cases, quasi-1D-like bands parallel to the k_x-axis with hole pockets at the Γ point can be obtained, being similar to the result obtained by high coverage hydrogen adsorption.[50] We note that recent ARPES experiments on $MoTe_2$ on a bilayer graphene shows similar FSs with doping.[17]

Fig. 3(a)–(i) represent phonon dispersions, phonon density of states (PHDOS), and Eliashberg spectral function ($\alpha^2F(\omega)$) of $MoTe_2$ and WTe_2 with varying n_{2D}. The most noticeable change upon electron doping is that at $\mathbf{q} \simeq \frac{4}{5}XM$ and $\frac{4}{5}\Gamma Y$ the low energy

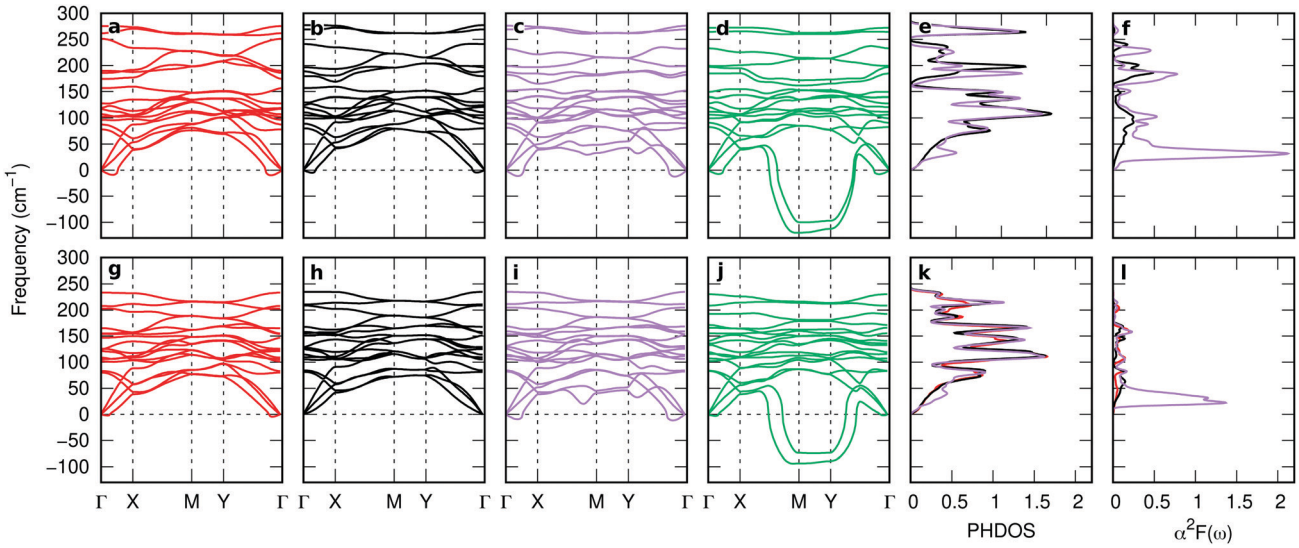

Fig. 3 Phonon dispersion of $MoTe_2$ for (a) $n_{2D} = -9.07 \times 10^{13}$ e cm^{-2} (hole doping), (b) pristine, (c) $n_{2D} = 1.36 \times 10^{14}$ e cm^{-2}, and (d) $n_{2D} = 3.63 \times 10^{14}$ e cm^{-2}. (e) Phonon density of states and (f) $\alpha^2F(\omega)$ for pristine and $n_{2D} = 1.36 \times 10^{14}$ e cm^{-2}. Phonon dispersion of WTe_2 with (g) $n_{2D} = -9.04 \times 10^{13}$ e cm^{-2}, (h) pristine, (i) $n_{2D} = 9.04 \times 10^{13}$ e cm^{-2}, and (j) $n_{2D} = 4.06 \times 10^{14}$ e cm^{-2}. (k) Phonon density of states and (f) $\alpha^2F(\omega)$ for pristine and $n_{2D} = 9.04 \times 10^{13}$ e cm^{-2}.

acoustic phonons were softened significantly. While the homogeneous background charge does not break inversion symmetry,[32] the FET gating lifts the degeneracy of phonon modes in the M–Y line. We also computed phonon frequencies of $MoTe_2$ in the vicinity of $\mathbf{q} = \frac{4}{5}XM$ with a fine $\mathbf{q}$-grid at n_{2D}= 1.80×10^{14} e cm^{-2} and confirmed that $\mathbf{q} = \frac{4}{5}XM$ has lower frequency than $\mathbf{q} = \frac{3}{4}XM$ as shown in Fig. S1 (ESI†). The computed phonon frequency at $\mathbf{q} = \frac{4}{5}XM$ is found to be -45.16 cm^{-1}, while it is found to be -42.10 cm^{-1} at $\mathbf{q} = \frac{3}{4}XM$. We also compared energy gain by the CDW formation with 2×5 and 2×8 phases which correspond to the $\mathbf{q} = \frac{4}{5}XM$ and $\mathbf{q} = \frac{3}{4}XM$, and found that the 2×5 CDW is more stable than the 2×8 CDW by $\sim$10 meV per 1×1 unitcell in a wide range of n_{2D} (see Fig. S2, ESI†). The PHDOS around 50 cm^{-1} is slightly increased and subsequently $\alpha^2F(\omega)$ is strongly enhanced, implying that the low energy acoustic phonon modes are responsible for the SC phase of doped $MoTe_2$ and WTe_2.

The calculated T_c of the SC phase using the Allen-Dynes formula, electron–phonon coupling constant (λ), and logarithmic average of phonon frequencies (ω_{log}) as a function of n_{2D} are plotted in Fig. 4. For pristine $MoTe_2$ (WTe_2) the calculated λ and T_c are 0.59 (0.33) and 1.039 (0.004) K, respectively. As n_{2D} increases, λ increases and ω_{log} decreases, showing the dome-shaped T–n diagram. The computed maximum T_c of $MoTe_2$ (WTe_2) reaches 9.16 (6.30) K at $n_{2D} = 1.36 \times 10^{14}$ (9.04×10^{13}) e cm^{-2}. It is reported that T_c of a pristine 1T′-$MoTe_2$ is 7.6 K,[11] and that for WTe_2 the $T_c \sim 1$ K at $n_{2D} \sim 1.8 \times 10^{13}$ e cm^{-1}.[10,29]

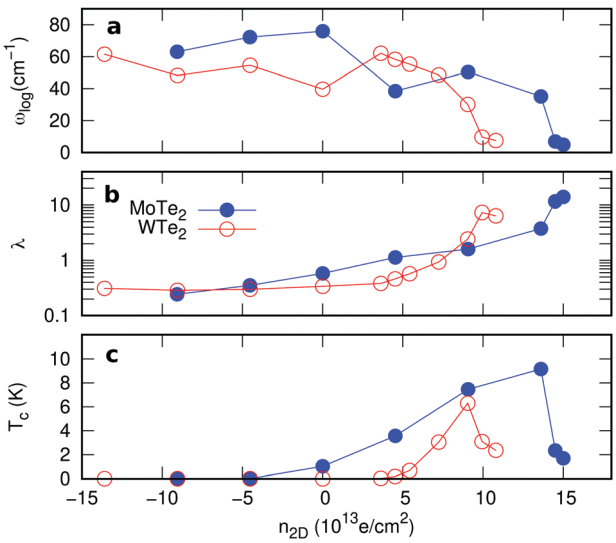

Fig. 4 (a) Logarithmic average of phonon frequencies (ω_{log}), (b) electron–phonon coupling constant (λ), and (c) superconducting transition temperature (T_c) for $MoTe_2$ (filled blue circles) and WTe_2 (open red circles) in a wide range of n_{2D}.

Our calculation results agree with the experiments qualitatively.[9–11] The over/underestimation of T_c can be found in doped MoS_2[21] and other materials too, due to limitations of the current theoretical approximations.[51,52] Although the observed maximum T_c in WTe_2 is $\sim$1 K for the available n_{2D} in the experiment, we anticipate that T_c could be enhanced if n_{2D} could be increased. For a hole doped region ($n_{2D} < 0$), there is no significant phonon softening and the calculated λ and T_c tend to be weakened, which is consistent with the experimental.[10] Based on our results, the SC in the gated single-layer $MoTe_2$ and WTe_2 can be attributed to the electron

doping-induced softening of the low energy acoustic phonon.[8–11] It is noteworthy that the softened acoustic phonon-induced SC is likely to be a universal mechanism for superconductivity in 2D TMDs.[21,53,54]

With further doping, the atomic structures of the both 1T′-$MoTe_2$ and 1T′-WTe_2 become unstable. When $n_{2D} \geq 1.40(1.03) \times 10^{14}$ e cm^{-2} for $MoTe_2$ (WTe_2), the frequencies of the softened acoustic phonon mode become negative around q_{CDW}, $\mathbf{q}_{CDW} \simeq \frac{4}{5}XM$. The lattice instability is relieved by forming a new stable structure in a 2 × 5 supercell with respect to the unit cell (called as 2 × 5 CDW hereafter) where the transition metals (TMs) along with zigzag chain direction (y) are distorted, as shown in Fig. 5(a). We plot the displacement of TMs along the y-direction (dy) for several n_{2D} in Fig. 5(b). Although the patterns of dy in $MoTe_2$ and WTe_2 differ a little, they together show the 2 × 5 CDW phase from the phonon instability at the same $\mathbf{q}_{CDW}$. There are weak lattice distortions in the vicinity of Mo_4 and Mo_6 of $MoTe_2$, while in WTe_2 the distortions are more significant. These distinctions could be ascribed to the difference in mass and the valence configuration of Mo and W atoms.[49] The largest dy of TMs in $MoTe_2$ (WTe_2) is ~6.4(4.6)% of the 1 × 1 lattice constant, implying the origin of the 2 × 5 CDW would be strong electron–phonon coupling rather than Fermi surface nesting.[5,55,56] It is noticeable that the lattice distortion in the 2 × 5 CDW phase respects a nonsymmorphic crystal symmetry as will be discussed later. For much higher $n_{2D} \sim 2.72(1.99) \times 10^{14}$ e cm^{-2} for $MoTe_2$ (WTe_2) $\mathbf{q}_{CDW}$ changes from $\frac{4}{5}XM$ to M as shown in Fig. 3(d) and (j). The M point is commensurate with a 2 × 2 supercell and we calculate 2 × 2 CDW phases in the same way as applied to the 2 × 5 CDW, as shown in Fig. 5(c) and (d).

We investigated the stability of the 2 × 5 and the 2 × 2 CDW phases by calculating their formation energy as a function of n_{2D}. Here we will consider a range, 9.04×10^{13} e cm^{-2} ≤ n_{2D} ≤ 4.53×10^{14} e cm^{-2}. The formation energy of $I \times j$ CDW states can be written as

$$\Delta E_{CDW}^{n_{2D}} \equiv \left(E_{i\times j}^{n_{2D}} - M \cdot E_{1\times 1}^{n_{2D}}\right)/M \quad (4)$$

where $E_{i\times j}^{n_{2D}}$ stands for the total energy of an $i \times j$ CDW phase, and $E_{1\times 1}^{n_{2D}}$ stands for the total energy of the 1 × 1 1T′ unitcell for a given doping of n_{2D} and $M \equiv i \times j$. Fig. 5(e) displays the $\Delta E_{CDW}^{n_{2D}}$ for $MoTe_2$ and WTe_2. The transition to the 2 × 5 CDW in WTe_2 takes place at lower n_{2D} than $MoTe_2$. For a given n_{2D}, the $\Delta E_{CDW}^{n_{2D}}$ of WTe_2 is larger than that of $MoTe_2$, implying the enhanced stability and a higher CDW transition temperature of WTe_2 than that of $MoTe_2$. When $n_{2D} \geq 2.90(1.90) \times 10^{14}$ e cm^{-2} for $MoTe_2$ (WTe_2), the $\Delta E_{CDW}^{n_{2D}}$ of the 2 × 2 CDW is more stable than that of the 2 × 5 CDW. The change of the relative stability between the two CDW phases coincides with the change of the instability $\mathbf{q}_{CDW}$ from $\frac{4}{5}XM$ to M. The n_{2D} region that can find the 2 × 5 CDW of WTe_2 is narrow compared to that of $MoTe_2$.

The new CDW phase of doped 1T′-TMDs shows interesting topological electronic properties owing to their crystal symmetries. Fig. 6(a) and (b) represent the electronic band structures of the 2 × 5 CDW of $MoTe_2$ for $n_{2D} = 2.27 \times 10^{14}$ e cm^{-2} and WTe_2 for $n_{2D} = 1.63 \times 10^{14}$ e cm^{-2}, respectively. The calculated $\Delta E_{CDW}^{n_{2D}}$ at these n_{2D} for $MoTe_2$ and WTe_2 are −13.11 meV and −7.71 meV, respectively. The crystal structure of the 2 × 5 CDW possesses nonsymmorphic symmetry that can be written as

$$\{g|t\} = \left\{M_{\hat{y}}|\frac{1}{2}0\right\} \quad (5)$$

where $g = M_{\hat{y}}$ is a glide mirror line (the gray solid line in Fig. 5(a) and dashed vertical lines in Fig. 5(b)), and $\mathbf{t} = \left(\frac{1}{2}, 0\right)$ is a half-translation along the x-axis. The nonsymmorphic symmetry without the inversion symmetry guarantees that the energy bands must have twofold-degenerated Weyl points along $M_{\hat{y}}$ invariant lines at $k_y = 0$ and π, even in the presence of the SOC as shown in Fig. 6(a) and (b).[36] Thanks to the FET condition considered here that allows us to make fractional band filling, we can place the Weyl points in the vicinity of the shifted E_F by gating. From the calculated band structures, we can infer that 1T′-$MoTe_2$ and WTe_2 are quite unique materials showing the

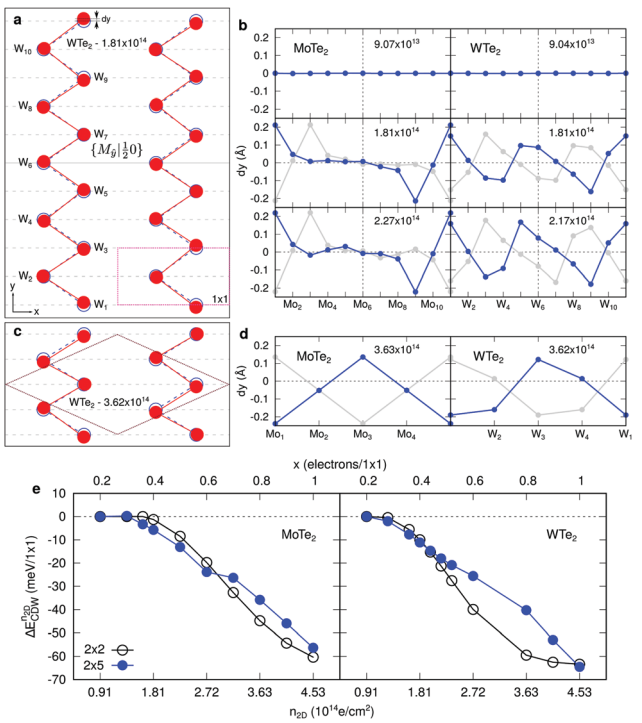

Fig. 5 Optimized positions of transition metals (TMs) in (a) 2 × 5 and (c) 2 × 2 CDW phases of WTe_2. Blue open circles represent TMs without lattice displacements. Pink dashed and gray solid lines in (a) represent the 1T′ unitcell and a glide mirror line ($M_{\hat{y}}$), respectively. Brown dashed lines in (c) represent a primitive cell of the 2 × 2 CDW. The displacements of TMs along the y axis for (b) the 2 × 5 and (d) the 2 × 2 CDW of $MoTe_2$ (left) and WTe_2 (right) are shown. Blue (gray) solid lines stand for the left (right) chain of TMs in (a) and (c). (e) Calculated CDW formation energies for $MoTe_2$ (left) and WTe_2 (right) as a function of n_{2D}. Black open (blue filled) circles represent the 2 × 2(2 × 5) CDW.

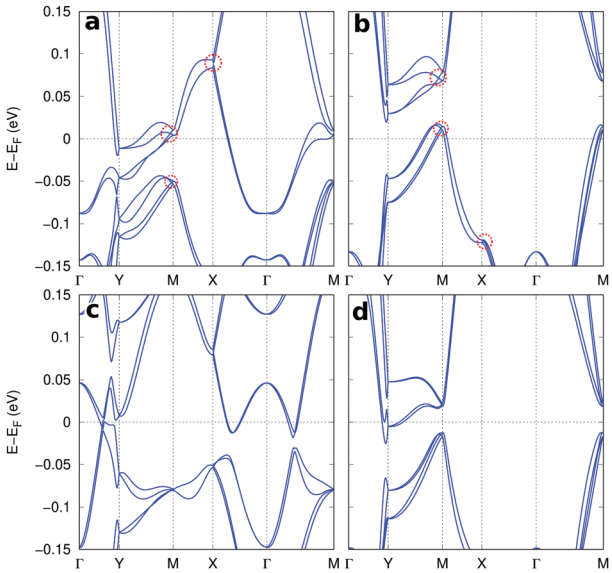

Fig. 6 Electronic band structures of 2 × 5 CDW phase with SOC at (a) n_{2D} = 2.27 × 10^{14} e cm^{-2} in $MoTe_2$, (b) n_{2D} = 1.63 × 10^{14} e cm^{-2} in WTe_2, (c) x = 4e/2 × 5 × 1 in $MoTe_2$, and (d) x= 4e/2 × 5 × 1 in WTe_2. Red dashed circles in (a) and (b) represent symmetry-protected twofold degenerated Weyl points.

2D Weyl in its doped single-layer and the 3D Weyl fermions in its stacked structure.[4]

The new 2 × 5 CDW phase coexists with the QSH state as the CDW energy bands are fully filled. We plotted the Mo d and Te p projected band structures of 2 × 5 CDW of $MoTe_2$ with n_{2D} of 1.81 × 10^{14} e cm^{-2} that corresponds to four electrons in the 2 × 5 × 1 supercell as shown in Fig. S3 (ESI†). We found that S_1 and S_2 bands at the Γ point [Fig. S3(a), ESI†] feature inverted band characters around E_F, similar to the pristine 1T′ WTe_2.[3] Here, no crossing points exist in the entire Brillouin zone because of the lack of inversion symmetry. As we include the SOC, the inverted bands develop Rashba splitting and form new hybridized bands as shown in Fig. 6(c) and (d), respectively. The calculated $\Delta E^{n_{2D}}_{CDW}$ at this n_{2D} for $MoTe_2$ and WTe_2 are −5.71 meV and −11.16 meV, respectively. Although the computed band structures show semimetallic character, we expect that the 2 × 5 CDW band structure can have a finite spectral gap between inverted bands when the environmental screening changes,[57] or when gentle external mechanical perturbations are applied. Following some experiments demonstrating substrate-induced tensile strain along the y axis,[3,16,17] we applied similar tensile strains along the same direction and computed band structures as shown in Fig. S4. We confirm that a band gap forms while preserving inverted band character (Fig. S4(a)–(c), ESI†). As we increase the strain more than 2%, the inverted band character disappears.

4 Conclusions

We theoretically demonstrate a series of phase transitions between the QSH state, SC phase, and CDW phase in gated monolayer 1T′-TMDs as a function of doped charges induced by the planar gate in a field effect transistor device set up, or equivalently homogeneous ionic gating. The newly found CDW states in partially filled $MoTe_2$ and WTe_2 are shown to coexist with a 2D Weyl semimetallic state thanks to nonsymmorphic crystal symmetry of the distorted CDW lattices. Furthermore, with fully filled bands, they re-entered the QSH insulating phase, coexisting with the CDW states. Considering various intriguing interfacial states realized between topological states and the superconducting phase such as Majorana fermions,[37–40] we believe that doping controlled electronic phase transitions in monolayer 1T′-TMDs shown here, could provide a new facile platform toward topological state engineering.

Conflicts of interest

There are no conflicts to declare.

Acknowledgements

We thank Sejoong Kim, Seoung-Hun Kang, Heejun Yang, Bohm-Jung Yang, and Thomas Brumme for fruitful discussions. Y.-W. S. was supported by the National Research Foundation (NRF) grant funded by the Korean government (MSIP) (Grant No. 2017R1A5A1014862, SRC program: vdWMRC center). The computing resources were supported by the Center for Advanced Computation (CAC) of KIAS.

Notes and references

1 J. A. Wilson, F. J. Di Salvo and S. Mahajan, *Adv. Phys.*, 2001, **50**, 1171–1248.
2 J. Wilson and A. Yoffe, *Adv. Phys.*, 1969, **18**, 193–335.
3 X. Qian, J. Liu, L. Fu and J. Li, *Science*, 2014, **346**, 1344–1347.
4 A. A. Soluyanov, D. Gresch, Z. Wang, Q. Wu, M. Troyer, X. Dai and B. A. Bernevig, *Nature*, 2015, **527**, 495–498.
5 M. Calandra, I. I. Mazin and F. Mauri, *Phys. Rev. B: Condens. Matter Mater. Phys.*, 2009, **80**, 241108.
6 X. Xi, L. Zhao, Z. Wang, H. Berger, L. Forró, J. Shan and K. F. Mak, *Nat. Nanotechnol.*, 2015, **10**, 765–769.
7 M. M. Ugeda, A. J. Bradley, Y. Zhang, S. Onishi, Y. Chen, W. Ruan, C. Ojeda-Aristizabal, H. Ryu, M. T. Edmonds, H.-Z. Tsai, A. Riss, S.-K. Mo, D. Lee, A. Zettl, Z. Hussain, Z.-X. Shen and M. F. Crommie, *Nat. Phys.*, 2016, **12**, 92.
8 Y. Saito, T. Nojima and Y. Iwasa, *Nat. Rev. Mater.*, 2017, **2**, 16094.
9 V. Fatemi, S. Wu, Y. Cao, L. Bretheau, Q. D. Gibson, K. Watanabe, T. Taniguchi, R. J. Cava and P. Jarillo-Herrero, *Science*, 2018, **362**, 926.
10 E. Sajadi, T. Palomaki, Z. Fei, W. Zhao, P. Bement, C. Olsen, S. Luescher, X. Xu, J. A. Folk and D. H. Cobden, *Science*, 2018, **362**, 922.
11 D. A. Rhodes, A. Jindal, N. F. Q. Yuan, Y. Jung, A. Antony, H. Wang, B. Kim, Y.-C. Chiu, T. Taniguchi, K. Watanabe,

K. Barmak, L. Balicas, C. R. Dean, X. Qian, L. Fu, A. N. Pasupathy and J. Hone, *Nano Lett.*, 2021, **21**, 2505.
12 Z. Lai, Q. He, T. H. Tran, D. V. M. Repaka, D.-D. Zhou, Y. Sun, S. Xi, Y. Li, A. Chaturvedi, C. Tan, B. Chen, G.-H. Nam, B. Li, C. Ling, W. Zhai, Z. Shi, D. Hu, V. Sharma, Z. Hu, Y. Chen, Z. Zhang, Y. Yu, X. Renshaw Wang, R. V. Ramanujan, Y. Ma, K. Hippalgaonkar and H. Zhang, *Nat. Mater.*, 2021, **20**, 1113.
13 M. Chhowalla, H. S. Shin, G. Eda, L.-J. Li, K. P. Loh and H. Zhang, *Nat. Chem.*, 2013, **5**, 263.
14 D. H. Keum, S. Cho, J. H. Kim, D.-H. Choe, H.-J. Sung, M. Kan, H. Kang, J.-Y. Hwang, S. W. Kim, H. Yang, K. J. Chang and Y. H. Lee, *Nat. Phys.*, 2015, **11**, 482.
15 Z. Fei, T. Palomaki, S. Wu, W. Zhao, X. Cai, B. Sun, P. Nguyen, J. Finney, X. Xu and D. H. Cobden, *Nat. Phys.*, 2017, **13**, 677.
16 S. Tang, C. Zhang, D. Wong, Z. Pedramrazi, H.-Z. Tsai, C. Jia, B. Moritz, M. Claassen, H. Ryu, S. Kahn, J. Jiang, H. Yan, M. Hashimoto, D. Lu, R. G. Moore, C.-C. Hwang, C. Hwang, Z. Hussain, Y. Chen, M. M. Ugeda, Z. Liu, X. Xie, T. P. Devereaux, M. F. Crommie, S.-K. Mo and Z.-X. Shen, *Nat. Phys.*, 2017, **13**, 683.
17 S. Tang, C. Zhang, C. Jia, H. Ryu, C. Hwang, M. Hashimoto, D. Lu, Z. Liu, T. P. Devereaux, Z.-X. Shen and S.-K. Mo, *APL Mater.*, 2018, **6**, 026601.
18 S. Wu, V. Fatemi, Q. D. Gibson, K. Watanabe, T. Taniguchi, R. J. Cava and P. Jarillo-Herrero, *Science*, 2018, **359**, 76–79.
19 H. W. Kim, S.-H. Kang, H.-J. Kim, K. Chae, S. Cho, W. Ko, S. Jeon, S. H. Kang, H. Yang, S. W. Kim, S. Park, S. Hwang, Y.-K. Kwon and Y.-W. Son, *Nano Lett.*, 2020, **20**, 5837–5843.
20 E. Morosan, H. W. Zandbergen, B. S. Dennis, J. W. G. Bos, Y. Onose, T. Klimczuk, A. P. Ramirez, N. P. Ong and R. J. Cava, *Nat. Phys.*, 2006, **2**, 544.
21 M. Rösner, S. Haas and T. O. Wehling, *Phys. Rev. B: Condens. Matter Mater. Phys.*, 2014, **90**, 245105.
22 Y. Yu, F. Yang, X. F. Lu, Y. J. Yan, Y.-H. Cho, L. Ma, X. Niu, S. Kim, Y.-W. Son, D. Feng, S. Li, S.-W. Cheong, X. H. Chen and Y. Zhang, *Nat. Nanotechnol.*, 2015, **10**, 270.
23 J. T. Ye, Y. J. Zhang, R. Akashi, M. S. Bahramy, R. Arita and Y. Iwasa, *Science*, 2012, **338**, 1193–1196.
24 Y. Ge and A. Y. Liu, *Phys. Rev. B: Condens. Matter Mater. Phys.*, 2013, **87**, 241408.
25 L. J. Li, E. C. T. O'Farrell, K. P. Loh, G. Eda, B. Özyilmaz and A. H. Castro Neto, *Nature*, 2016, **529**, 185.
26 M. Kan, J. Y. Wang, X. W. Li, S. H. Zhang, Y. W. Li, Y. Kawazoe, Q. Sun and P. Jena, *J. Phys. Chem. C*, 2014, **118**, 1515–1522.
27 Y. Li, K.-A. N. Duerloo, K. Wauson and E. J. Reed, *Nat. Commun.*, 2016, **7**, 10671.
28 W. Zan, Z. Hu, Z. Zhang and B. I. Yakobson, *Nanoscale*, 2016, **8**, 19154.
29 W. Zan, Z. Zhang, Y. Yang, X. Yao, S. Li and B. I. Yakobson, *Nanotechnology*, 2019, **30**, 075701.
30 Y.-C. Lin, D. O. Dumcenco, Y.-S. Huang and K. Suenaga, *Nat. Nanotechnol.*, 2014, **9**, 391.
31 Y. Wang, J. Xiao, H. Zhu, Y. Li, Y. Alsaid, K. Y. Fong, Y. Zhou, S. Wang, W. Shi, Y. Wang, A. Zettl, E. J. Reed and X. Zhang, *Nature*, 2017, **550**, 487.
32 W. Yang, C. J. Mo, S. B. Fu, Y. Yang, F. W. Zheng, X. H. Wang, Y. A. Liu, N. Hao and P. Zhang, *Phys. Rev. Lett.*, 2020, **125**, 237006.
33 Y. M. Xie, B. T. Zhou and K. T. Law, *Phys. Rev. Lett.*, 2020, **125**, 107001.
34 X. Xi, Z. Wang, W. Zhao, J. H. Park, K. T. Law, H. Berger, L. Forró, J. Shan and K. F. Mak, *Nat. Phys.*, 2016, **12**, 139.
35 T. Brumme, M. Calandra and F. Mauri, *Phys. Rev. B: Condens. Matter Mater. Phys.*, 2014, **89**, 245406.
36 S. M. Young and C. L. Kane, *Phys. Rev. Lett.*, 2015, **115**, 126803.
37 L. Fu and C. L. Kane, *Phys. Rev. Lett.*, 2008, **100**, 096407.
38 L. Fu and C. L. Kane, *Phys. Rev. B: Condens. Matter Mater. Phys.*, 2009, **79**, 161408.
39 S. Hart, H. Ren, T. Wagner, P. Leubner, M. Mühlbauer, C. Brüne, H. Buhmann, L. W. Molenkamp and A. Yacoby, *Nat. Phys.*, 2014, **10**, 638.
40 V. S. Pribiag, A. J. A. Beukman, F. Qu, M. C. Cassidy, C. Charpentier, W. Wegscheider and L. P. Kouwenhoven, *Nat. Nanotechnol.*, 2015, **10**, 593.
41 P. Giannozzi, S. Baroni, N. Bonini, M. Calandra, R. Car, C. Cavazzoni, D. Ceresoli, G. L. Chiarotti, M. Cococcioni, I. Dabo, A. Dal Corso, S. de Gironcoli, S. Fabris, G. Fratesi, R. Gebauer, U. Gerstmann, C. Gougoussis, A. Kokalj, M. Lazzeri, L. Martin-Samos, N. Marzari, F. Mauri, R. Mazzarello, S. Paolini, A. Pasquarello, L. Paulatto, C. Sbraccia, S. Scandolo, G. Sclauzero, A. P. Seitsonen, A. Smogunov, P. Umari and R. M. Wentzcovitch, *J. Phys.: Condens. Matter*, 2009, **21**, 395502.
42 P. Giannozzi, O. Andreussi, T. Brumme, O. Bunau, M. B. Nardelli, M. Calandra, R. Car, C. Cavazzoni, D. Ceresoli, M. Cococcioni, N. Colonna, I. Carnimeo, A. Dal Corso, S. de Gironcoli, P. Delugas, R. A. DiStasio Jr., A. Ferretti, A. Floris, G. Fratesi, G. Fugallo, R. Gebauer, U. Gerstmann, F. Giustino, T. Gorni, J. Jia, M. Kawamura, H.-Y. Ko, A. Kokalj, E. Küçükbenli, M. Lazzeri, M. Marsili, N. Marzari, F. Mauri, N. L. Nguyen, H.-V. Nguyen, A. O. de-la Roza, L. Paulatto, S. Poncé, D. Rocca, R. Sabatini, B. Santra, M. Schlipf, A. P. Seitsonen, A. Smogunov, I. Timrov, T. Thonhauser, P. Umari, N. Vast, X. Wu and S. Baroni, *J. Phys.: Condens. Matter*, 2017, **29**, 465901.
43 J. P. Perdew, K. Burke and M. Ernzerhof, *Phys. Rev. Lett.*, 1996, **77**, 3865–3868.
44 D. R. Hamann, *Phys. Rev. B: Condens. Matter Mater. Phys.*, 2013, **88**, 085117.
45 J. Noffsinger, F. Giustino, B. D. Malone, C. H. Park, S. G. Louie and M. L. Cohen, *Comput. Phys. Commun.*, 2010, **181**, 2140.
46 S. Poncé, E. R. Margine, C. Verdi and F. Giustino, *Comput. Phys. Commun.*, 2016, **209**, 116.
47 F. Giustino, M. L. Cohen and S. G. Louie, *Phys. Rev. B: Condens. Matter Mater. Phys.*, 2007, **76**, 165108.
48 M. Kawamura, *Comput. Phys. Commun.*, 2019, **239**, 197.
49 H.-J. Kim, S.-H. Kang, I. Hamada and Y.-W. Son, *Phys. Rev. B*, 2017, **95**, 180101.
50 J. Seok, J.-H. Lee, S. Cho, B. Ji, H. W. Kim, M. Kwon, D. Kim, Y.-M. Kim, S. H. Oh, S. W. Kim, Y. H. Lee, Y.-W. Son and H. Yang, *2D Mater.*, 2017, **4**, 025061.

51 Z. Li, G. Antonius, M. Wu, F. H. Da Jornada and S. G. Louie, *Phys. Rev. Lett.*, 2019, **122**, 186402.
52 Z. Li, M. Wu, Y.-H. Chan and S. G. Louie, *Phys. Rev. Lett.*, 2021, **126**, 146401.
53 C. Heil, S. Poncé, H. Lambert, M. Schlipf, E. R. Margine and F. Giustino, *Phys. Rev. Lett.*, 2017, **119**, 087003.
54 J. Simonin, *Phys. Rev. B: Condens. Matter Mater. Phys.*, 1986, **33**, 7830.
55 K. Rossnagel, *J. Phys.: Condens. Matter*, 2011, **23**, 213001.
56 M. D. Johannes and I. I. Mazin, *Phys. Rev. B: Condens. Matter Mater. Phys.*, 2008, **77**, 165135.
57 J. Ryou, Y.-S. Kim, S. Kc and K. Cho, *Sci. Rep.*, 2016, **6**, 29184.